NOTE

Magnetic Resonance in Medicine 00:000–000 (2013)

Background Field Removal Using Spherical Mean Value Filtering and Tikhonov Regularization

Hongfu Sun and Alan H. Wilman*

Purpose: To introduce a new method for removing background artifacts in field maps and apply it to enhance the accuracy of susceptibility mapping.

Methods: A field artifact removal method is introduced that is based on the sophisticated harmonic artifact reduction for phase data (SHARP) method exploiting the harmonic mean value property. The new method uses Tikhonov regularization at the deconvolution stage and is referred to as regularization enabled SHARP (RESHARP). RESHARP was compared with SHARP in a field-forward susceptibility simulation and in human brain experiments, considering effects on both field maps and the resulting susceptibility maps.

Results: From the simulation, RESHARP was able to reduce error in the field map by 17.4% as compared with SHARP, resulting in a more accurate single-angle susceptibility map with 6.5% relative error (compared with 48.5% using SHARP). Using RESHARP in vivo, field and susceptibility maps of the brain displayed fewer artifacts particularly at the brain boundaries, and susceptibility measurements of iron-rich deep gray matter were also more consistent than SHARP across healthy subjects of similar age.

Conclusion: Compared with SHARP, RESHARP removes background field artifact more effectively, leading to more accurate susceptibility measurements in iron-rich deep gray matter. **Magn Reson Med 000:000–000, 2013. © 2013 Wiley Periodicals, Inc.**

Key words: phase imaging; background artifact; SHARP; Tikhonov regularization; susceptibility mapping; brain iron

Magnetic susceptibility provides a valuable source of MRI contrast to distinguish iron-rich brain structures from surrounding tissue. Although the magnetic field shifts in susceptibility-weighted imaging (1,2) and phase imaging (3) can reflect regional susceptibility features, they do not represent the exact local susceptibility distribution due to the nonlocal source-to-field relationship (4). Furthermore, the induced magnetic field depends on the object orientation to the main magnetic field (5,6), raising an additional problem for quantitative assessment (7). Quantitative susceptibility mapping attempts to overcome the field direction dependence and the nonlocal nature of traditional phase imaging by means of a deconvolution on the field map to recover the underlying local source susceptibility distribution (8–16). Quantitative susceptibility mapping is being promoted as a promising and accurate means for brain iron mapping (17,18). Unfortunately, the inversion from field perturbation to susceptibility is ill-conditioned, which means that noise or artifacts in the field map can be substantially amplified in the resulting susceptibility map. Therefore, an effective removal of background field is a prerequisite for successful quantitative susceptibility mapping.

Background field is considered as any field contribution from sources other than local tissue susceptibility including eddy currents, chemical shifts, receiver radiofrequency offsets and, most notably, air-tissue susceptibility interfaces at the skull and sinuses. Different removal methods have been proposed, such as high pass filtering (19), polynomial fitting (20,21), and field-forward estimation (22). However, these methods tend either to leave residual background field, or to attenuate local field in the process. Recently, two other promising techniques exploiting the physics property of susceptibility dipole sources have been proposed: Projection onto dipole field (23) and sophisticated harmonic artifact reduction for phase data (SHARP) (13). The former models a hypothetical distribution of background susceptibility sources that provides the closest fit to the total field. The latter uses the mean value property (24) to separate the harmonic background field from the nonharmonic local field. Improvements to SHARP may be possible by introducing Tikhonov regularization (25), which has been previously applied to quantitative susceptibility mapping (10,11). In this work, an improved background field removal method is presented by applying Tikhonov regularization at the deconvolution stage of spherical mean value filtering (i.e., SHARP). The new method, referred to as regularization enabled SHARP (RESHARP), is validated through a numerical phantom simulation and parameter-optimized for human brain experiments. It is compared with traditional SHARP, considering effects on both the field maps and the resulting susceptibility maps.

THEORY

Harmonic Background Field and Mean Value Property

The principles used in SHARP (13) are briefly reviewed below. According to the Maxwell's equations, the dipole field induced by susceptibility sources outside the

Department of Biomedical Engineering, University of Alberta, Edmonton, Canada.

Grant sponsors: Canadian Institutes of Health Research (CIHR) and Natural Sciences and Engineering Research Council of Canada (NSERC).

*Correspondence to: Alan H. Wilman, Ph.D., Department of Biomedical Engineering, University of Alberta, 1098 RTF, Edmonton, Alberta T6G 2V2, Canada. E-mail: alan.wilman@ualberta.ca

Received 16 January 2013; revised 25 February 2013; accepted 21 March 2013

DOI 10.1002/mrm.24765
Published online in Wiley Online Library (wileyonlinelibrary.com).

region-of-interest (ROI) is harmonic within the ROI (26), hence satisfying the mean value property (24):

$$M\big((\ \delta\ -\ \rho\ ) \otimes B_{\text{bkg}}\big) = 0, \quad [1]$$

where ρ is a nonnegative, radially symmetric, normalized convolution kernel (entries within the sphere summed to 1; values outside the sphere were uniformly 0); δ denotes the Dirac delta function; B_{bkg} is the harmonic background field; M is the binary brain mask defining the ROI as the brain volume (value 1 within ROI, value 0 elsewhere) but is further eroded by the radius of ρ due to the violation of the mean value property whenever ρ overlaps with the brain edge. The convolution can be reformulated more intuitively as a multiplication in the Fourier domain:

$$MF^{-1}CFB_{\text{bkg}} = 0, \quad [2]$$

where F denotes the Fourier transform matrix; $C = \mathcal{F}(\delta - \rho)$ is the convolution kernel after Fourier transform ($\mathcal{F}$). By multiplying $MF^{-1}CF$ by the total field B_{total}, the background field component is removed, leaving only the local field component to be solved as written below:

$$MF^{-1}CFB_{\text{local}} = MF^{-1}CFB_{\text{total}}. \quad [3]$$

In the original SHARP method (13), Eq. [3] is relaxed at the boundary of the eroded ROI by abandoning M from the local field term, written as $F^{-1}CFB_{\text{local}} = MF^{-1}CFB_{\text{total}}$, then solved with truncated singular value decomposition (SVD): setting the frequency of the expected local field to zero whenever the corresponding value of C is beneath a user-determined threshold value.

RESHARP with Tikhonov Regularization

The system of Eq. [3] is underdetermined and therefore extra information is required to obtain a unique solution. Since the susceptibility difference between air and water/tissue is more than an order of magnitude larger than the inter-tissue variation due to brain iron, myelin, and deoxyhemoglobin (27), background field is assumed to be the predominate component of the measured total field, hence, the residual local field component with least-norm is chosen specifically as the desired solution.

Seeking the least-norm solution from Eq. [3] is a constrained minimization problem, and the method of Lagrange multiplier (28) is commonly used to convert it to a well-developed unconstrained minimization form. In the RESHARP method, this Lagrangian form is formulated by adding the Tikhonov regularization (norm of the solution) to the data fidelity term (norm of the misfit residual), and balancing with the Lagrange multiplier as written below:

$$\text{argmin}_{B_{\text{local}}} ||MF^{-1}CF(B_{\text{local}} - B_{\text{total}})||_2^2 + \lambda\ ||B_{\text{local}}||_2^2 \quad [4]$$

In the above formula, $\text{argmin}_{B_{\text{local}}}$ denotes the values of variable B_{local} that minimize the above function; $||\cdots||_2^2$ denotes the sum of squares; the first norm term is the data fidelity term to guarantee the harmonic assumption of background field; the second term is the Tikhonov regularization term to enhance the small norm feature of the residual local field after background field removal; λ is the Lagrange multiplier (regularization parameter) to be set such that the norm of the local field is minimal while subject to data fidelity within expected error tolerance. To determine the optimal Lagrange multiplier, a range of λ values are first assigned to Eq. [4], and then the minimization is solved for each λ. The norm of the data fidelity term (i.e., misfit residual) is plotted against the solution norm $\left(||B_{\text{local}}||_2^2\right)$ for the range of tested λ and the λ corresponding to the point of maximal curvature is considered optimal (L-curve (29)).

METHODS

Numerical Simulation

A modified Shepp-Logan phantom (30) (128 × 128 × 128 pixels) representing a susceptibility distribution was created, with five ellipsoids of varying sizes to simulate uniform-intensity structures and an internal sphere to simulate an air cavity. The background air outside the phantom and within the inner spherical cavity were assigned a susceptibility of 9.4 ppm (27); the five ellipsoids were assigned susceptibilities of 0.05, 0.1, 0.15, 0.2, and 0.3 ppm, similar to values found in brain; and the susceptibility of the remaining region was set to 0 simulating a water/tissue reference (Fig. 1a–c). The induced local field from the five ellipsoids and the background field from the air-tissue interfaces were forwardly calculated (Fig. 1d–f) by convolving with the unit dipole kernel (31–33).

Human Brain Experiments

Three-dimensional multiple gradient-echo datasets covering the whole brain were acquired at 4.7 T (Varian, Palo Alto, CA) from five subjects (all male, age 48 ± 3 years). The studies were conducted with the approval of our Institutional Review Board. A head coil transmitter and a four-channel receiver array were used. Acquisition parameters were: field of view = 25.6 × 16 × 16 cm^3; spatial resolution = 1 × 1 × 2 mm^3; bandwidth = 352 Hz/voxel; pulse repetition time = 40 ms; echo time = 3/7/11/15/19 ms; flip angle = 10°.

Phase measurements from the four receiver channels were first optimally combined accounting for the radiofrequency offsets (34), followed by unwrapping using PRELUDE/FSL (35–37). Then, a voxel-wise magnitude-weighted least-squares regression of phase to echo time was performed to obtain the reduced-noise field map (38,39). A field reliability mask was also generated by setting a threshold for the regression residual, with corrupted fields of large residuals (greater than threshold) set to 0 while others set to 1. The threshold was selected by visual inspection such that unreliable voxels were generally confined to the edges of the ROI and scarcely present within it. The regression was performed on normalized field maps (relative to the main magnetic field), and the threshold was selected as 1×10^{-3} then applied across subjects. Unreliable field measurements were then excluded from the ROI by multiplying the reliability mask to the field map before continuing to the next steps.

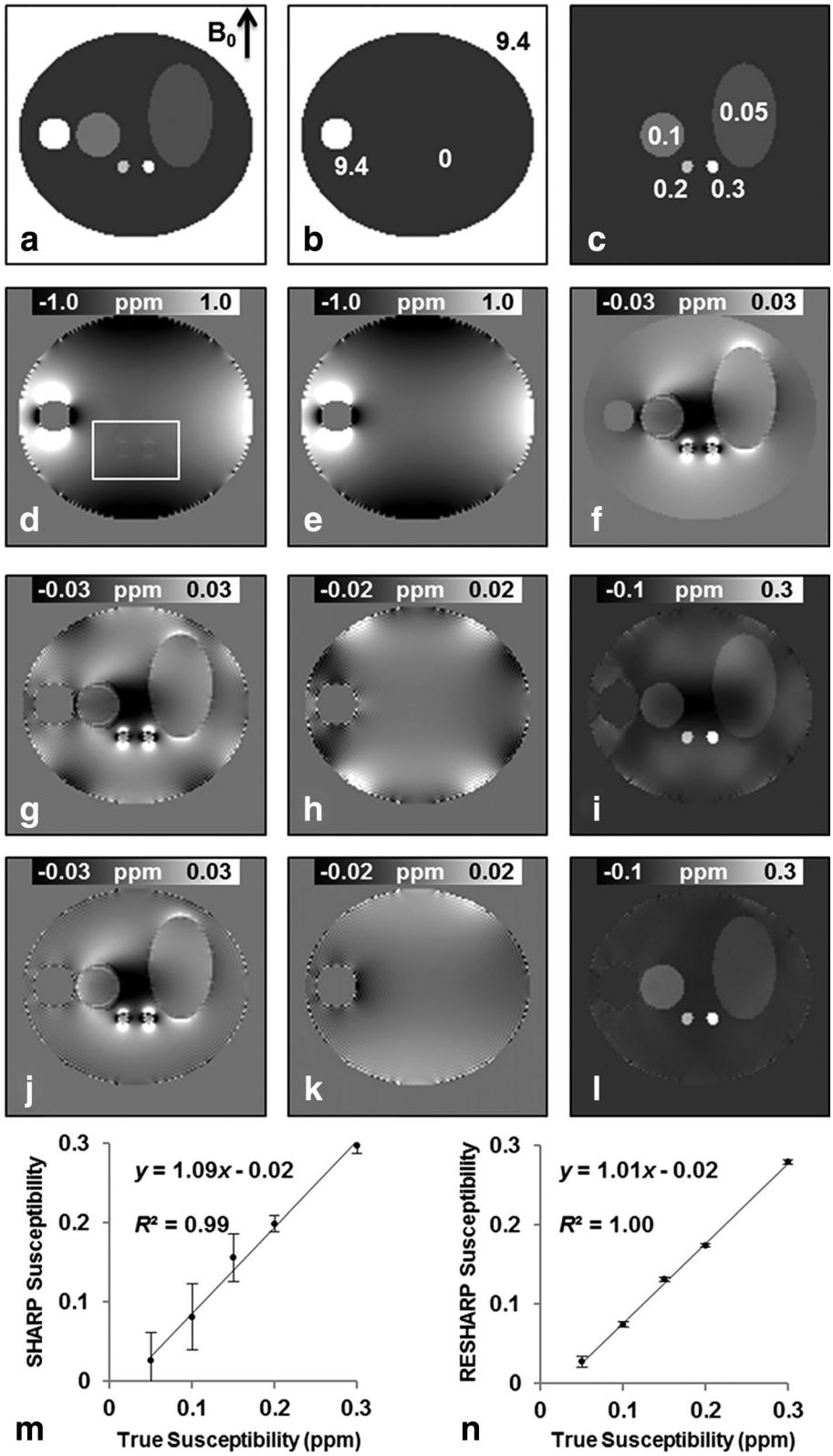

FIG. 1. Simulation results from a three-dimensional ellipsoidal Shepp-Logan phantom. The total susceptibility distribution from the central coronal slice of the phantom is shown in (**a**), consisting of background susceptibility differences (**b**) and local susceptibility differences (**c**), with susceptibility values assigned to them in units of ppm. Induced total field, background field, and local field are displayed in (**d**), (**e**), and (**f**), respectively. Local field maps filtered from SHARP and RESHARP are displayed in (**g**) and (**j**), with their error differences to the true local field displayed in (**h**) and (**k**). The susceptibility maps from SHARP and RESHARP field maps are shown in (**i**) and (**l**). Mean values of five inner ellipsoids relative to the mean value of the remaining reference territories are also plotted against true susceptibility values in (**m**) for SHARP and (**n**) for RESHARP.

Background Field Removal with RESHARP/SHARP

The radius of the spherical convolution kernel ρ was chosen as five voxels (40). The binary mask defining the brain volume was extracted using brain extraction tool (BET) (41) from the magnitude images of the first echo. The eroded mask M was then computed by convolving the BET mask with ρ: resulting voxels of value 1 were retained as M, while others were set to value 0. For the RESHARP method, the minimization of Eq. [4] was achieved using the linear conjugate gradient method

with the stopping criterion chosen as the relative residual smaller than 10^{-6}. As illustrated in Figure 2, to avoid either under- or over-regularization, λ was selected according to the L-curve method (29) along with simple visual inspection to ensure that artifacts were suppressed as much as possible without incurring significant loss in tissue contrast. Using this technique, a λ of 5×10^{-3} was determined from one human subject and then applied to the other four subjects. For the SHARP method, the truncation level was set to 0.05 (40) which led to best suppression of artifacts by visual inspection and was consistent with the value used in the SHARP paper (13).

Susceptibility Inversion with Total Variation Regularization

In the original SHARP paper (13), field to susceptibility inversion was performed using the multiple-angle acquisition method (8). However, in this work, we used a more practical single-angle acquisition method, and the susceptibility maps were reconstructed using the total variation regularization approach (15,42). The regularization parameter on the total variation term was selected as 5×10^{-4} which was determined from a single subject using the L-curve and remained the same for the other subjects.

RESULTS

Numerical Simulation

The simulation results of background field removal are shown in Figure 1. The local field map from SHARP (Fig. 1g) displays alternating bright-dark patterns at the boundary—easily identified as artifacts in the error map (Fig. 1h). In comparison, the local field from RESHARP (Fig. 1j) is free of these artifacts with no obvious pattern in the error map (Fig. 1k). Relative to the norm of total field, the norm of local field error is 2.18% for SHARP and 1.80% for RESHARP (i.e., 17.4% error decrease). The susceptibility map obtained from the SHARP result (Fig. 1i) displays large intensity variation within the ellipsoids (of constant susceptibility in the model) and particularly in the surrounding reference territory, while susceptibility obtained from the RESHARP (Fig. 1l) displays greater uniformity in these structures. Linear regressions of the measured mean susceptibilities versus the original model susceptibilities for the five ellipsoids yield a slope of 1.09 for SHARP (Fig. 1m) and 1.01 for RESHARP (Fig. 1n). Standard deviation of susceptibility measurements within each ellipsoid is much smaller for RESHARP (Fig. 1m) with relative error of 6.5% than SHARP (Fig. 1n) of 48.5% accounting for all the ellipsoids.

Human Brain Experiments

The local field maps of a human brain from RESHARP are displayed in Figure 2 for a range of regularization parameters λ in Eq. [4]. From the graph, the data fidelity term increases while the regularization term decreases with the parameter, and an L-curve is formed. Choosing a parameter that is too small, e.g., 5×10^{-5}, results in an under-regularized local field solution as seen in Figure 2a, where the frontal head in particular is severely

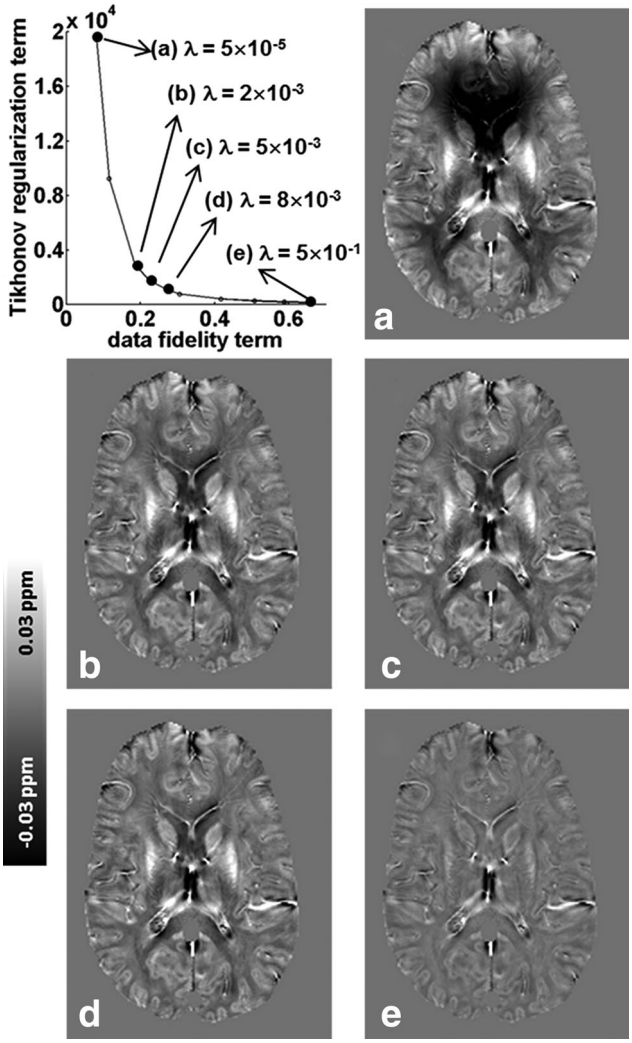

FIG. 2. The selection of proper regularization parameters for RESHARP. In the graph, the data fidelity term is plotted against the Tikhonov regularization term for a wide range of regularization parameters. The local field result from a small λ value of 5×10^{-5} is shown in (**a**), optimal λ values 2×10^{-3} (**b**), 5×10^{-3} (**c**), 8×10^{-3} (**d**), and a large λ value 5×10^{-1} in (**e**).

contaminated by artifact. Conversely, setting the parameter as large as 5×10^{-1}, results in an over-regularized solution, as seen in Figure 2e where severe artifacts are suppressed, but local field gray-white matter and tissue-iron contrast drop significantly. When the proper regularization parameter is selected around the corner of the L-curve, e.g., 5×10^{-3}, as shown in Figure 2c, the local field map is smoothly and symmetrically distributed, without obvious artifact, and white and gray matter territories are clearly discernible. Results from another two parameters around the L-curve corner, 2×10^{-3} (Fig. 2b) and 8×10^{-3} (Fig. 2d), demonstrated little change compared with 5×10^{-3} (Fig. 2c).

Comparisons of SHARP and RESHARP from the human brain study are shown in Figure 3. Artifacts present in the SHARP field map (indicated by the white arrows in Fig. 3a) are concentrated at the boundaries of the brain. Field maps obtained from RESHARP (Fig. 3b)

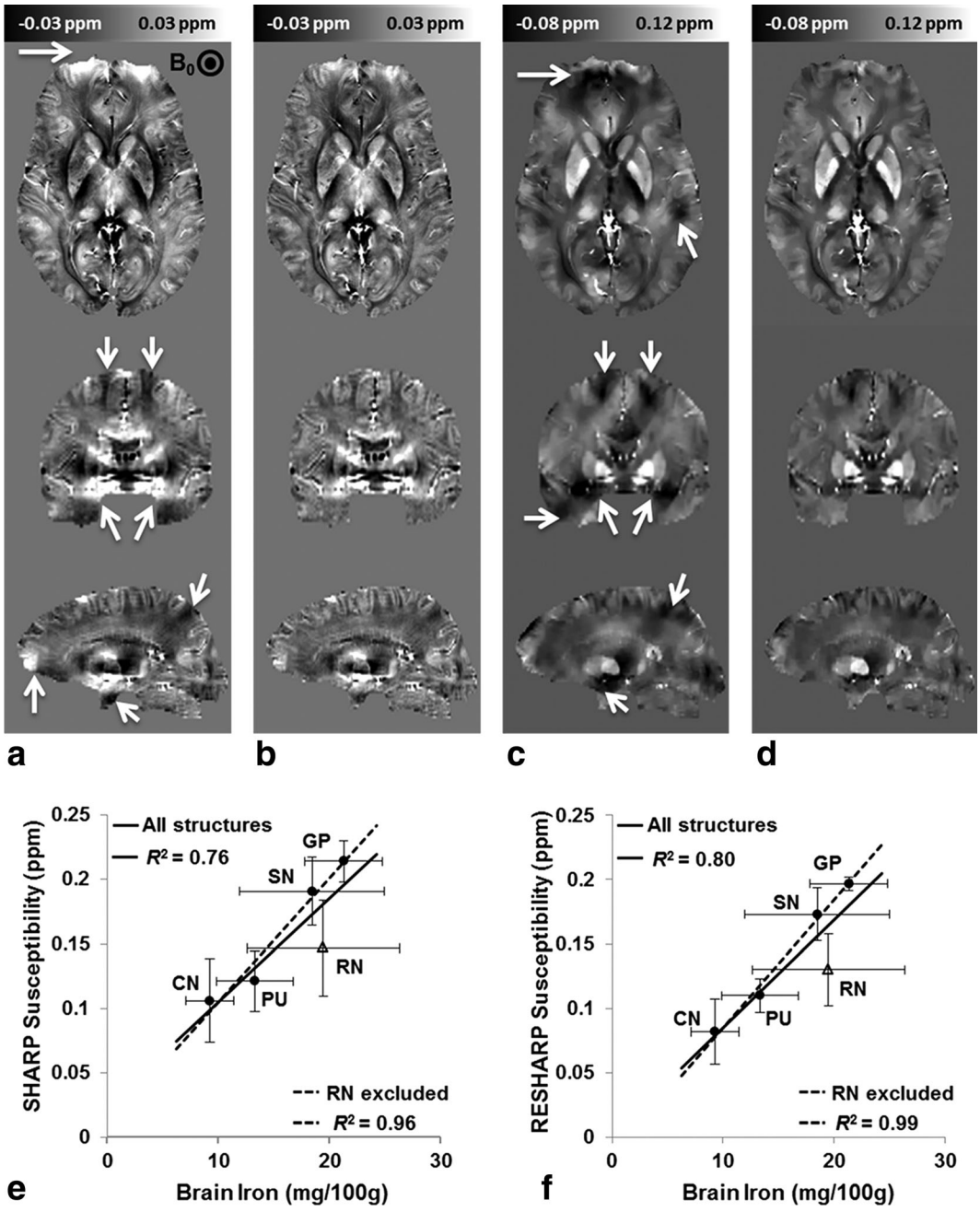

FIG. 3. Human brain comparison of SHARP and RESHARP on a 45-year-old male. Images are shown in transverse, coronal, and sagittal views within each column. Local field maps are shown from (**a**) SHARP and (**b**) RESHARP. Susceptibility maps inversed from (a) and (b) are shown in column (**c**) and (**d**) correspondingly. White arrows point at areas with strong artifacts in both field and susceptibility maps when using SHARP. Regressions of averaged susceptibility values (Mean ± SD) to the estimated brain iron concentrations of deep gray matter regions from five healthy males are shown in (**e**) using SHARP and (**f**) using RESHARP. Regressions including all five globus pallidus (GP), putamen (PU), caudate nucleus (CN), red nucleus (RN), and substantia nigra (SN) are indicated in solid lines and with RN excluded in dashed lines.

show artifacts substantially suppressed or completely removed in the corresponding areas. Susceptibility maps calculated from the SHARP local field (Fig. 3c) show residual streaking and severe artifact, as indicated by the white arrows, evidently resulting from residual background artifact remaining in the field map. Susceptibility maps obtained from RESHARP results (Fig. 3d) exhibit reduced artifact and better tissue contrast, with distinct delineation of the iron-rich deep gray matter.

The plots of measured susceptibility values against brain iron concentrations estimated from the Hallgren and Sourander study (43) are shown in Figure 3e for SHARP and Figure 3f for RESHARP. Two-dimensional ROIs for each structure were drawn manually using central transverse slices. Measured susceptibilities of deep gray matter structures were normalized (subtraction) relative to the measured cerebrospinal fluid susceptibility for each subject. Mean values and standard deviations of normalized

deep gray matter susceptibilities were then calculated among the five subjects. The linear correlation for RESHARP ($R^2 = 0.80$) is slightly higher than that for SHARP ($R^2 = 0.76$) as indicated by solid regression lines. The susceptibility value range of RN estimated from Hallgren and Sourander study is quite different from a more recent study by Krebs et al. (44). In addition, iron concentrations of RN measured by Krebs et al. also present very large variations among individuals. If excluding the measurements of RN from regressions (triangle markers), the linear correlations of the other four structures increase substantially for both methods as indicated by dashed regression lines, with that from RESHARP ($R^2 = 0.99$) still slightly higher than that from SHARP ($R^2 = 0.96$). More importantly, the standard deviations of the five mean measurements from RESHARP are substantially smaller than those from SHARP, which means RESHARP measurements of individual structures are more consistent across subjects of similar age.

DISCUSSION

Both from an image quality perspective and from quantitative error analysis, field maps and susceptibility results from the numerical simulation and human brain experiments demonstrate that RESHARP was superior to SHARP in background field removal and gave improved performance for single-angle susceptibility inversion.

RESHARP and SHARP have two major differences. First, in the SHARP method, the M term defining the eroded ROI in Eq. [3] is dropped, and the equation is approximated as $F^{-1}CFB_{\text{local}} = MF^{-1}CFB_{\text{total}}$ to perform SVD, and the initial solution was then multiplied by M as the final B_{local} solution. In the RESHARP method, Eq. [3] was not relaxed as in SHARP and the solution was obtained by conjugate gradient iterations. Our simulation results showed that RESHARP performed better at the boundary (defined by M term) than SHARP. Second, SHARP uses truncated SVD while RESHARP uses Tikhonov regularization to suppress noise/error amplification. Briefly, the filter factor of truncated SVD is a harsh rectangular function, while in Tikhonov regularization it is a similar but much smoother function. In human brain experiments, low frequency residual radiofrequency-offsets as well as unwrapping errors compounded in the field map (not modeled by susceptibility background) could be largely amplified due to the small coefficients of the convolution kernel (C in Eq. [3]) in the low frequency regions, and a proper regularization is needed. In theory, truncated SVD induces more Gibbs artifacts than Tikhonov regularization due to the harsh truncation of the filter factor. This was observed in our human brain results, RESHARP performed better than SHARP in terms of suppressing artifacts.

A current limitation of both SHARP and RESHARP is the erosion of the ROI by an amount equal to the radius of the convolution kernel, thereby losing local field (and susceptibility) information at the brain boundary. In this work, we chose a radius of five voxels (40), which we believe was the optimal kernel size considering both fidelity and integrity of the result. Fortunately, the erosion of the ROI does not influence the susceptibility measurements of deep gray matter. To further reduce the amount of boundary loss, a varying kernel size scheme was proposed whereby the kernel size was gradually reduced approaching the ROI boundary (15). Projection onto dipole field (23) is an alternative method that does not involve the erosion of the boundary. Instead, it works by fitting susceptibility sources outside the ROI to reproduce the background field within it. However, the comparison with projection onto dipole field is beyond the scope of this note.

In conclusion, an improved background field removal method RESHARP has been presented that builds on the SHARP method by using Tikhonov regularization at the deconvolution stage of spherical mean value filtering. It has been shown through simulation and human brain experiments that this method is more effective at removing background field than original SHARP, leading to susceptibility maps with suppressed artifact and more accurate quantitative susceptibility measurements in iron-rich deep gray matter.

REFERENCES

1. Haacke EM, Mittal S, Wu Z, Neelavalli J, Cheng YC. Susceptibility-weighted imaging: technical aspects and clinical applications, part 1. AJNR Am J Neuroradiol 2009;30:19–30.
2. Haacke EM, Xu Y, Cheng YC, Reichenbach JR. Susceptibility weighted imaging (SWI). Magn Reson Med 2004;52:612–618.
3. Rauscher A, Sedlacik J, Barth M, Mentzel HJ, Reichenbach JR. Magnetic susceptibility-weighted MR phase imaging of the human brain. AJNR Am J Neuroradiol 2005;26:736–742.
4. Jackson JD, Fox RF. Classical electrodynamics. Am J Phys 1999;67:841.
5. Schafer A, Wharton S, Gowland P, Bowtell R. Using magnetic field simulation to study susceptibility-related phase contrast in gradient echo MRI. Neuroimage 2009;48:126–137.
6. Marques JP, Maddage R, Mlynarik V, Gruetter R. On the origin of the MR image phase contrast: an in vivo MR microscopy study of the rat brain at 14.1 T. Neuroimage 2009;46:345–352.
7. Walsh AJ, Wilman AH. Susceptibility phase imaging with comparison to R2 mapping of iron-rich deep grey matter. Neuroimage 2011;57:452–461.
8. Liu T, Spincemaille P, de Rochefort L, Kressler B, Wang Y. Calculation of susceptibility through multiple orientation sampling (COSMOS): a method for conditioning the inverse problem from measured magnetic field map to susceptibility source image in MRI. Magn Reson Med 2009;61:196–204.
9. Shmueli K, de Zwart JA, van Gelderen P, Li TQ, Dodd SJ, Duyn JH. Magnetic susceptibility mapping of brain tissue in vivo using MRI phase data. Magn Reson Med 2009;62:1510–1522.
10. Kressler B, de Rochefort L, Liu T, Spincemaille P, Jiang Q, Wang Y. Nonlinear regularization for per voxel estimation of magnetic susceptibility distributions from MRI field maps. IEEE Trans Med Imaging 2010;29:273–281.
11. de Rochefort L, Liu T, Kressler B, Liu J, Spincemaille P, Lebon V, Wu J, Wang Y. Quantitative susceptibility map reconstruction from MR phase data using bayesian regularization: validation and application to brain imaging. Magn Reson Med 2010;63:194–206.
12. Wharton S, Bowtell R. Whole-brain susceptibility mapping at high field: a comparison of multiple- and single-orientation methods. Neuroimage 2010;53:515–525.
13. Schweser F, Deistung A, Lehr BW, Reichenbach JR. Quantitative imaging of intrinsic magnetic tissue properties using MRI signal phase: an approach to in vivo brain iron metabolism? Neuroimage 2011;54:2789–2807.
14. Liu J, Liu T, de Rochefort L, et al. Morphology enabled dipole inversion for quantitative susceptibility mapping using structural consistency between the magnitude image and the susceptibility map. Neuroimage 2012;59:2560–2568.
15. Wu B, Li W, Guidon A, Liu C. Whole brain susceptibility mapping using compressed sensing. Magn Reson Med 2012;67:137–147.
16. Bilgic B, Pfefferbaum A, Rohlfing T, Sullivan EV, Adalsteinsson E. MRI estimates of brain iron concentration in normal aging using quantitative susceptibility mapping. Neuroimage 2012;59:2625–2635.

17. Langkammer C, Schweser F, Krebs N, et al. Quantitative susceptibility mapping (QSM) as a means to measure brain iron? A post mortem validation study. Neuroimage 2012;62:1593–1599.
18. Reichenbach JR. The future of susceptibility contrast for assessment of anatomy and function. Neuroimage 2012;62:1311–1315.
19. Rauscher A, Barth M, Herrmann KH, Witoszynskyj S, Deistung A, Reichenbach JR. Improved elimination of phase effects from background field inhomogeneities for susceptibility weighted imaging at high magnetic field strengths. Magn Reson Imaging 2008;26: 1145–1151.
20. Duyn JH, van Gelderen P, Li TQ, de Zwart JA, Koretsky AP, Fukunaga M. High-field MRI of brain cortical substructure based on signal phase. Proc Natl Acad Sci USA 2007;104:11796–11801.
21. Walsh AJ, Eissa A, Blevins G, Wilman AH. Susceptibility phase imaging with improved image contrast using moving window phase gradient fitting and minimal filtering. J Magn Reson Imaging 2012;36:1460–1469.
22. Neelavalli J, Cheng YC, Jiang J, Haacke EM. Removing background phase variations in susceptibility-weighted imaging using a fast, forward-field calculation. J Magn Reson Imaging 2009;29:937–948.
23. Liu T, Khalidov I, de Rochefort L, Spincemaille P, Liu J, Tsiouris AJ, Wang Y. A novel background field removal method for MRI using projection onto dipole fields (PDF). NMR Biomed 2011;24: 1129–1136.
24. Kim J, Wong M. Invariant mean value property and harmonic functions. Complex Variables Theory Appl 2005;50:1049–1059.
25. Tikhonov AN, Arsenin VIA, John F. Solutions of ill-posed problems. Washington: V. H. Winston; 1977.
26. Li L, Leigh JS. Quantifying arbitrary magnetic susceptibility distributions with MR. Magn Reson Med 2004;51:1077–1082.
27. Schenck JF. The role of magnetic susceptibility in magnetic resonance imaging: MRI magnetic compatibility of the first and second kinds. Med Phys 1996;23:815–850.
28. Lasdon LS. Optimization theory for large systems. New York: Dover Publications; 2002.
29. Hansen PC. The L-curve and its use in the numerical treatment of inverse problems. IMM, Department of Mathematical Modelling, Technical University of Denmark; 1999.
30. Jain AK. Fundamentals of digital image processing. Englewood Cliffs, NJ: Prentice Hall; 1989.
31. Marques J, Bowtell R. Application of a Fourier-based method for rapid calculation of field inhomogeneity due to spatial variation of magnetic susceptibility. Concepts Magn Reson B Magn Reson Eng 2005;25:65–78.
32. Salomir R, De Senneville BD, Moonen CTW. A fast calculation method for magnetic field inhomogeneity due to an arbitrary distribution of bulk susceptibility. Concepts Magn Reson B Magn Reson Eng 2003;19:26–34.
33. Koch KM, Papademetris X, Rothman DL, de Graaf RA. Rapid calculations of susceptibility-induced magnetostatic field perturbations for in vivo magnetic resonance. Phys Med Biol 2006;51:6381–6402.
34. Robinson S, Grabner G, Witoszynskyj S, Trattnig S. Combining phase images from multi-channel RF coils using 3D phase offset maps derived from a dual-echo scan. Magn Reson Med 2011;65:1638–1648.
35. Jenkinson M. Fast, automated, N-dimensional phase-unwrapping algorithm. Magn Reson Med 2003;49:193–197.
36. Smith SM, Jenkinson M, Woolrich MW, Beckmann CF, Behrens TEJ, Johansen-Berg H, Bannister PR, De Luca M, Drobnjak I, Flitney DE. Advances in functional and structural MR image analysis and implementation as FSL. Neuroimage 2004;23:S208–S219.
37. Woolrich MW, Jbabdi S, Patenaude B, Chappell M, Makni S, Behrens T, Beckmann C, Jenkinson M, Smith SM. Bayesian analysis of neuroimaging data in FSL. Neuroimage 2009;45(1 Suppl):S173–S186.
38. Gilbert G, Savard G, Bard C, Beaudoin G. Quantitative comparison between a multiecho sequence and a single-echo sequence for susceptibility-weighted phase imaging. Magn Reson Imaging 2012;30: 722–730.
39. Wu B, Li W, Avram AV, Gho SM, Liu C. Fast and tissue-optimized mapping of magnetic susceptibility and T2* with multi-echo and multi-shot spirals. Neuroimage 2012;59:297–305.
40. Schweser F, Sommer K, Atterbury M, Deistung A, Lehr BW, Reichenbach JR. On the impact of regularization and kernel type on SHARP-corrected GRE phase images. In Proceedings of the 19th Annual Meeting of ISMRM, Montreal, Canada, 2011. p. 2667.
41. Smith SM. Fast robust automated brain extraction. Hum Brain Mapp 2002;17:143–155.
42. Lustig M, Donoho D, Pauly JM. Sparse MRI: the application of compressed sensing for rapid MR imaging. Magn Reson Med 2007;58:1182–1195.
43. Hallgren B, Sourander P. The effect of age on the non-haemin iron in the human brain. J Neurochem 1958;3:41–51.
44. Krebs N, Langkammer C, Goessler W, Fazekas F, Yen K, Ropele S, Scheurer E. Brain iron: comparison of postmortem SWI with chemical tissue analysis. In Proceedings of the 18th Annual Meeting of ISMRM, Stockholm, Sweden, 2010. p. 702.